



ELSEVIER

Ultramicroscopy 70 (1997) 57–81

ultramicroscopy

Distortion correction of tubular crystals: improvements in the acetylcholine receptor structure

Rameen Beroukhim, Nigel Unwin*

MRC Laboratory of Molecular Biology, Hills Road, Cambridge CB2 2QH, UK

Received 30 May 1997; received in revised form 22 July 1997

Abstract

Biological molecules often crystallize either as tubes, having helical symmetry, or as two-dimensional sheets. Both sorts of crystal are potentially suitable for structure determination to atomic resolution by electron crystallography, but their lattice distortions must first be corrected. We have developed a procedure for tubular crystals, based on independent alignment of very short segments against a reference structure, that allows accurate determination and correction of distortions in all three dimensions. Application of this procedure to images used previously to determine the 9 Å structure of the acetylcholine receptor showed that about half of the signal loss caused by the distortions arises from effects correctable in the image plane (bending, changes in scale) and half from effects requiring out-of-plane correction (variations in tilt and in twist around the tube axis). By dividing the tubes into short segments (of lengths about equal to their diameter) it became possible to recover almost all of this loss without reducing appreciably the accuracy in the segmental alignments. The signal retention improved by only 10% at low resolution (20 Å), but by progressively greater amounts at higher resolutions, up to ~40% at 9 Å. As a result the finer structural details were more clearly resolved. With images of better electron-optical quality, much greater gains in signal retention should be obtained.

Keywords: Distortion correction; Tubular crystals; Acetylcholine receptor

1. Introduction

Tubular crystals are assemblies of identical molecules arranged periodically over the surface of a cylinder to make a helix. Membrane proteins and also some soluble proteins form these crystals through protein–protein interactions or through specific associations involving the lipids. One of the

best-characterized examples is the tube formed by the nicotinic acetylcholine (ACh) receptor [1], a neurotransmitter-gated ion channel involved in the transmission of electrical signals between cells at the chemical synapse. Other examples include calcium ATPase [2], botulinum neurotoxin [3], RNA polymerase [4], the cytochrome bc_1 complex [5], and photosystem II [6]. Such tubes are often no more than ~1000 Å across: sufficiently thin, when embedded in ice, to be imaged in the electron microscope as weak phase object [7]. Compared with helical filaments, tubes contain more subunits

* Corresponding author. Tel.: 01223-402492; Fax: 01223-402310.

and therefore more information per unit length. Unlike two-dimensional crystals they present views of their constituent molecules from many different, precisely defined directions. Tubes therefore appear to be exceptionally favorable specimens for three-dimensional structure determination by electron crystallography.

Despite their advantages, however, the best resolution attained from tubes is only $\sim 9 \text{ \AA}$. The presence of distortions is one limiting factor. Distortions cause regions of a crystal to be displaced from their exact lattice positions, leading to reduction of diffraction intensities and signal loss, which become progressively greater at higher resolution. Correction of displacements in two-dimensional lattices, due to bending in the image plane, has been shown to bring about substantial improvements in signal-to-noise ratio [8], allowing in some cases atomic detail to be revealed [9, 10]. With tubes, large displacements can arise from bending in the image plane, tilting (bending away from the image plane), variations in twist around the tube axis, changes in scale due to slight stretching or shrinkage, and flattening in the direction parallel to the electron beam. Since the best images are obtained from tubes lying over holes in the carbon support film [11], rather than on the flat film itself, the three-dimensional distortions – tilt and twist – are likely to be particularly important. Several procedures have been devised for correcting some of these distortions in other helical assemblies: for example, bending within the image plane has been corrected by reinterpolating the image point-for-point in studies of actin filaments [12–14], tobacco mosaic virus [15], RecA filaments [16], microtubules [17, 18], and bacterial flagellar filaments [19, 20]; variable twist has been corrected by applying an innovative real-space algorithm in a study of sickle cell hemoglobin fibers [21]. However, no way has yet been developed that corrects the different kinds of distortions at the same time.

We describe here a general method that simultaneously corrects the different kinds of distortions. The tube is first divided into very short segments; each segment is independently aligned in all three dimensions by cross-correlation against a reference structure; and then the individual segments are

added together after the distortion-induced displacements between them have been removed. This method thus treats each short segment as a perfect helix, ignoring any small displacements caused by the distortions within the segment. As discussed in the next section, the recentering of the tube at intervals should greatly reduce the large displacements incurred by most long-range distortions (bending, scale changes, variable tilt and twist). By using short enough segments, all displacements (including those within segments, which are not corrected) are reduced to the point they no longer have a significant effect.

The effectiveness of this approach (like any other) depends on the precision with which the distortions can be locally determined. If the segment length is too long, the variations along the tube will be smeared out (poor local fitting). If the segment length is too short, any gain resulting from improving the fitting to the reference structure (i.e. by following the distortions more closely with shorter steps) might be outweighed by the new losses incurred by increased alignment errors (due to the lower signal-to-noise ratios of such short segments).

To evaluate the method and the properties of distortions present in tubular crystals, we investigated the images used in an earlier study that determined the 9 \AA structure of the nicotinic ACh receptor [22]. We are able to show that about half of the signal loss caused by distortions in the ACh receptor tubes arises from effects correctable in two-dimensions (bending and scale changes) and about half from effects requiring three-dimensional correction (i.e., variations in out-of-plane tilt and twist). By dividing the tubes into segments of length about equal to their diameter it was possible to recover almost all of this loss. Gains in signal retention increased to $\sim 40\%$ in the highest resolution range ($11\text{--}9 \text{ \AA}$), and extrapolations suggest that the distortion corrections should lead to much more substantial improvements when better images are obtained.

2. Theoretical considerations

In this section we examine the relation between the signal retained or lost and the length of the tube

segment. We calculate the amount of signal loss caused by a given type of distortion by first modeling the effects of the distortion on the crystal in real space, and then relating those effects to a reduction in the amplitude (or square root of intensity) of the signal in Fourier space.

Normally in investigating a crystal, one assumes that its component molecules are ordered in a regular array and, based on the lattice parameters of the array, one can predict where each element of mass in each molecule should be. Distortions, however, move those elements of mass away from their predicted positions, introducing errors in their alignment. When one takes the Fourier transform of the crystal, each element in the crystal contributes Fourier terms throughout the transform, all with particular amplitudes and phases. By moving one element of mass away from where it should be, we introduce a phase error into each of its Fourier terms:

$$\Delta\phi = 2\pi \frac{\Delta d}{\lambda_d}, \quad (1)$$

where $\Delta\phi$ is the phase error in radians of the Fourier term, Δd is the real-space error in the position of the mass (its displacement), and λ_d is the Δd -direction component of the Fourier term's wave vector.

In the transform of a perfect crystal, the Fourier terms from equivalent elements in different unit cells add up coherently at the layer-lines, where we collect the data. In a distorted crystal, the summation is no longer perfectly coherent: the strength of each term is reduced by the factor $\cos \Delta\phi$. So, looking at the whole crystal, the distortion-induced reduction in the amplitude of a particular Fourier term along a layer-line is

$$\text{Fraction retained} = \frac{\int_A \cos \Delta\phi(x, y) \, dx \, dy}{\int_A \cos 0 \, dx \, dy}, \quad (2)$$

where A covers the entire area of the crystal and $\Delta\phi(x, y)$ refers to the phase error of the Fourier term arising from the mass at (x, y) . (A , x , and y refer to the undistorted crystal.) To be exact, we should really integrate over the volume of the crys-

tal and weight each volume element by the mass it contains, but for a general idea of how distortions affect the data, this simplification should do. $\Delta\phi$, which is a function of the distortion-induced displacement (Eq. (1)), depends on the type of distortion and the displacements that the distortion induces.

Most distortions can be regarded as second-order effects: they generate displacements that accrue as the square of the distance from the center of the crystal. In tubes, bending within the image plane, stretch (or shrinkage) along the axis, and twist around the axis fall into the category of second-order distortions, since linear changes in the displacements they generate would only represent errors of overall alignment (see Appendix). The displacements accrue along the tube axis (y) more than they accrue normal to the axis (x) because of the tube's limited width, so the most damaging second-order distortions follow the general rule:

$$\Delta d = \zeta y^2, \quad (3)$$

where Δd is the positional error and ζ is a coefficient describing the magnitude of the distortion. Hence the fraction of signal retained, in the direction of maximum error, is related to the tube length by

$$\text{Fraction retained} = \frac{1}{\ell} \int_{-\ell/2}^{\ell/2} \cos \left(\frac{2\pi\zeta y^2}{\lambda} \right) dy, \quad (4)$$

where ℓ is the length of the segment and λ is the Fourier term's wavelength in the direction being considered. Fig. 1a illustrates the form of the curve for second-order distortions. Almost all the signal is retained for segments shorter than a critical length. Beyond this length, however, the retention drops off dramatically until a level corresponding to $\sim 20\%$ is reached, at which point the retention falls off more gradually. We find that the critical length for retention of 5 \AA detail with the ACh receptor tubes is typically $\sim 2000 \text{ \AA}$, and Fig. 1b shows the curve that would be obtained for this case.

Fig. 1c plots the curve calculated for retention of 5 \AA detail in the ACh receptor tubes, assuming first-order distortions: where the displacements accrue proportionally with distance. At their worst,

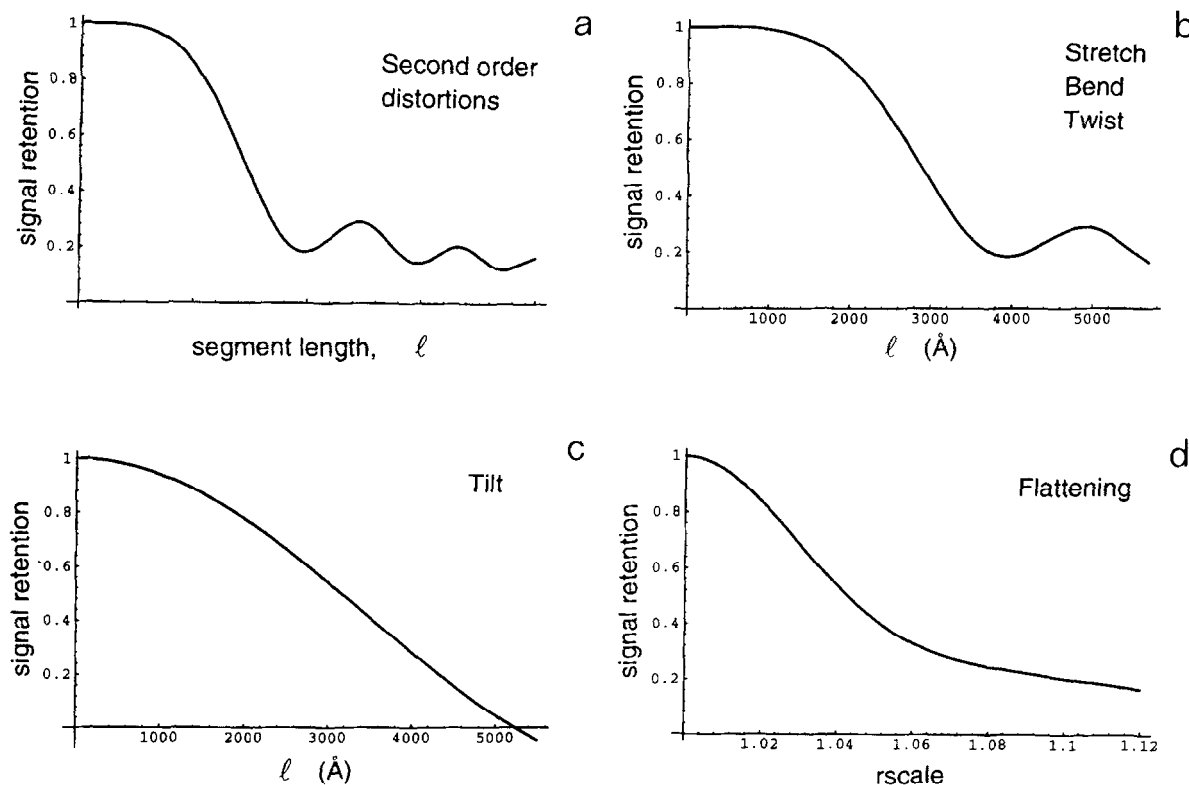


Fig. 1. Theoretical plots of fraction of signal retained as a function of segment length, l , (a–c), and flattening ratio, r_{scale} (d). (a) shows the form of the curve for second-order distortions, which include bending within the image plane, stretch (or shrinkage) along the tube axis, and azimuthal twist around this axis: almost all the signal is retained for segments shorter than a critical length; beyond this length, however, the signal retention drops off rapidly until it levels off again at $\sim 20\%$. (b) is a typical case for second-order distortions of ACh receptor tubes, where the critical length is ~ 2000 Å for retention of 5 Å detail. (c) is the case for retention of 5 Å detail with first-order distortions, which include variation in out-of-plane tilt: signal retention falls steadily as the length of the segment is increased; with short segments, however, most of the signal is still retained. (d) shows that rate of signal loss due to flattening (which is independent of the length of the segment) depends on the flattening ratio (r_{scale}); most of the signal is retained when the tube is flattened by less than 1–2%; 5% flattening, however, results in the loss of over half the signal. The r_{scale} value estimated experimentally corresponds to $r_{\text{scale}}(r_0)$ in the Appendix. The fractional signal retention was calculated in (b)–(d) in the direction of maximum displacement, using the equations in the Appendix (parameters for (c): $t = 3 \times 10^{-6}$, $n = 10$, $X = 0.005 \text{ \AA}^{-1}$, $Z = 0.2 \text{ \AA}^{-1}$; and for (d): $r_{\text{min}} = 250 \text{ \AA}$, $r_{\text{max}} = 380 \text{ \AA}$).

changes in out-of-plane tilt may be regarded as a distortion of this type, since (unlike positional displacements) linear changes in angular displacements cannot be represented simply as alignment errors. In this case, the amount of signal retained decreases more rapidly as the segment length is increased; however, most of the signal will still be retained if the segment is kept sufficiently short.

The amount of signal retained in flattened tubes depends solely on the extent of flattening, rather than on the segment length, so this distortion can-

not readily be corrected by dividing tube into shorter segments. However, most of the signal should be retained if the tube is flattened by less than 1–2% (Fig. 1d), a situation that appears likely to be fulfilled in images of narrow tubes which are completely surrounded by uniformly thick ice (see Section 5).

The main conclusion to be drawn from these calculations is that it is important to use segments of tube less than a critical length in the distortion analysis in order to avoid serious signal loss due to

most distortions, which are usually second- (or higher-) order effects. On the other hand, there is little to be gained by the use of segments much shorter than the critical length, because at this length the signal loss from even first-order distortions has already become quite small.

3. Methods

3.1. ACh receptor tubes

The tubes examined in this study were grown from the ACh receptor-rich postsynaptic membranes of the electric ray, *Torpedo marmorata* [1] and belong to a well characterized helical family (–16, 6); [11, 22–24]. They are composed of ACh receptors in their native lipid/protein environment, have a diameter of 770 Å, and are up to several microns long.

The images were of the tubes suspended in uniformly thick amorphous ice over holes in the carbon support film. Twenty-six of the images had been used in an earlier study to determine the structure of the ACh receptor at 9 Å [22], and were recorded at 35000× with a total dose of ~6 electron/Å², using a Philips EM420 microscope operating at 120 kV. Their range of defocus (7000–18 800 Å) was sufficiently wide to ensure that all spacings present were well sampled. A maximum range of 1.0–1.035 was allowed for the radial factor (rscale) needed to provide consistent scaling of any particular image with the reference dataset. Two additional images, recorded at 400 kV, were included in the analysis (i.e. 28 were used altogether). The micrographs were scanned with a modified Joyce-Loebl densitometer using spot and step sizes of 5 µm (corresponding to 1.43 Å on the specimen).

Approximate defocus and astigmatism values for the images were determined by sector-averaging of the amplitudes in Fourier transforms computed from the tubes, and by fitting of the averaged amplitudes in each sector to theoretical contrast transfer functions (CTFs), assuming a figure of 7% for the amplitude contrast [7, 25]. The CTF variation was later refined by comparing the phases of the Fourier terms from the near and far sides of each tube (corresponding to the sides nearest and fur-

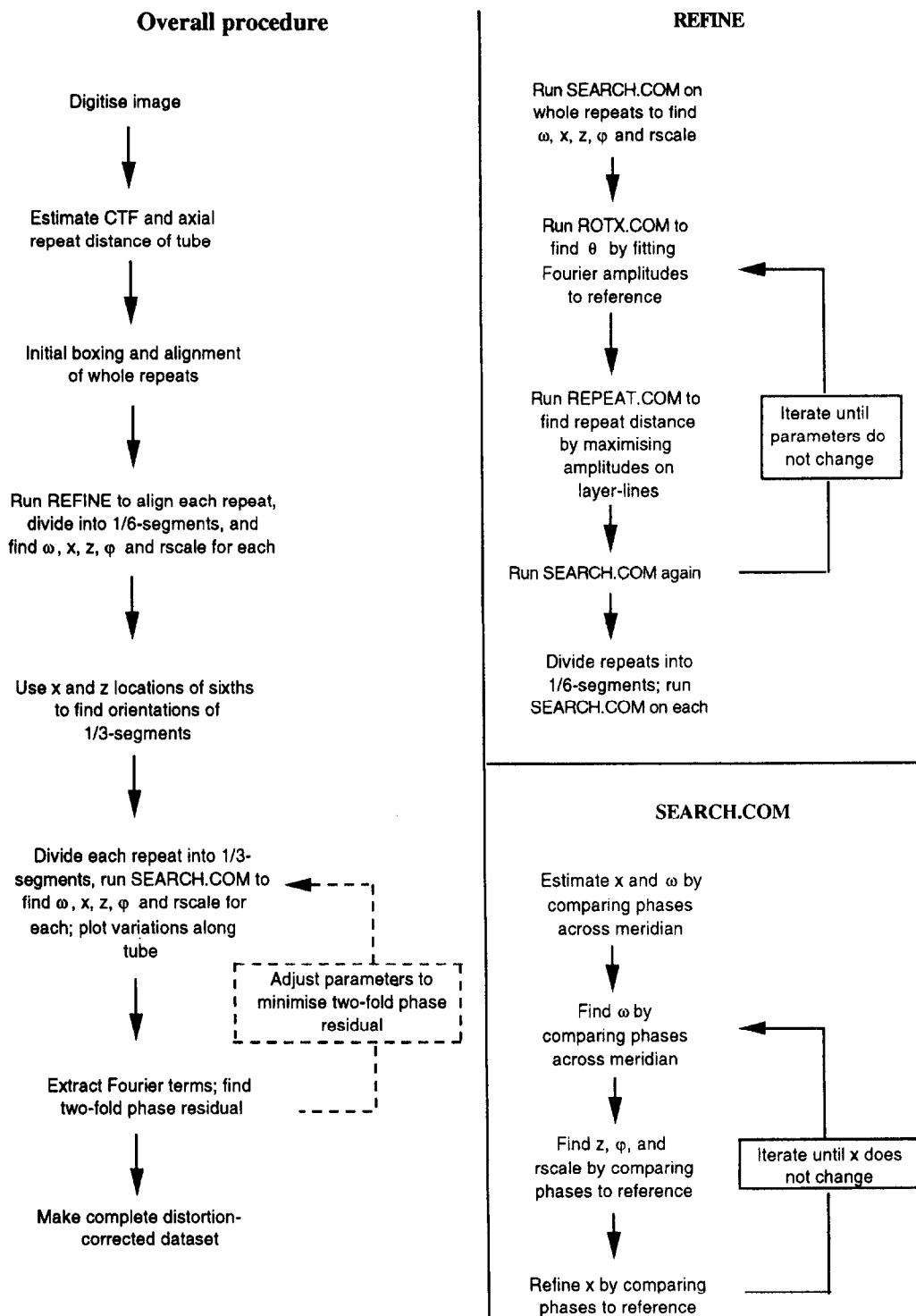
thest from the electron source) against those of a reference structure. This refinement, and other steps where the methods have been modified from previous work, are described in further detail below.

3.2. Subdivision of axial repeats

The axial repeat distances of most of the tubes had been determined in the earlier study, and were found to lie typically in the range 2000–4000 Å. Pilot studies suggested that segments about 800–1200 Å long were sufficiently short to be able to trace accurately the variations associated with each of the distortions, and that there was no advantage in using even shorter segments. We therefore chose a third of a whole repeat distance to be the standard subdivision into segments for alignment against the reference structure (although alternative subdivisions, maintaining for example approximately equal segment lengths, could readily be done). Each $\frac{1}{3}$ -segment was aligned independently of the others (see below), and the Fourier terms extracted from the $\frac{1}{3}$ -segments were recombined to re-create the (distortion-corrected) whole repeats. By using segments that were fixed fractions of the repeat length (rather than of constant length) and re-creating the whole repeats, we ensured that each distortion-corrected dataset contained information from a complete set of equally sampled views. If this were not done, there would be an increase in layer-line overlap which, in turn, would introduce errors in some of the higher resolution Fourier terms.

3.3. Distortion correction procedure

Fig. 2 gives a schematic outline of the steps involved in correcting distortions. The aim of the steps is to divide the whole repeats into $\frac{1}{3}$ -segments and to define completely the three-dimensional alignment of each $\frac{1}{3}$ -segment; that is, its rotation in the image plane (θ); out-of-plane tilt (ω); effective repeat length ('repeat'); width relative to that of the reference structure (rscale); and the x -, z - and azimuthal alignments (x , z , ϕ) of the origin (see Fig. 3). Each of these seven parameters, except for ω , is ultimately measured by comparing the Fourier terms obtained from the $\frac{1}{3}$ -segments with the



reference set of Fourier terms. The reference set used here was from the 9 Å structure [22], obtained by averaging the terms from 26 tubes.

The overall procedure (Fig. 2, left) is begun by dividing the (previously selected) best regions of the tube into lengths equal to the axial repeat distance.

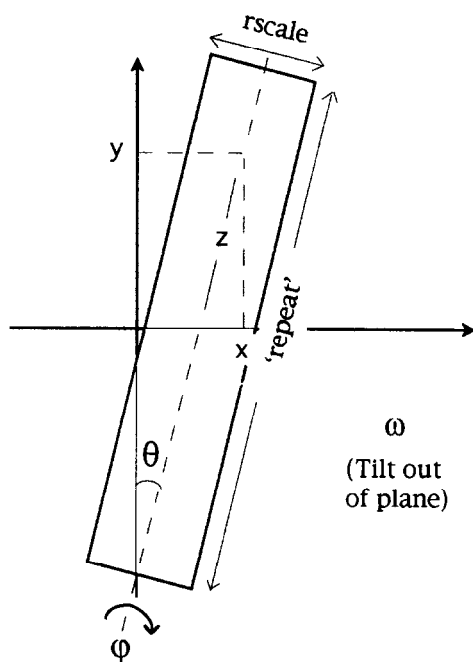


Fig. 3. Definitions of the alignment parameters describing a tube segment. θ is its orientation within the image plane (rotation); ω is its orientation out of the plane (tilt); x and y are the horizontal and vertical positions of the center of the segment; z is the distance of the origin from the x axis, along the tube; φ is the azimuthal location of the origin (twist); $rscale$ is the width of the tube relative to that of the reference structure; and 'repeat' is the length of tube that would contain all possible views of its component molecules.

Fig. 2. Flow chart for segment-by-segment correction of distortions in images of tubular crystals. Whole repeat lengths of the tubes are divided into $\frac{1}{3}$ -segments, which are aligned in three dimensions to a reference structure by determining their rotation in the image plane (θ); out-of-plane tilt (ω), effective repeat length ('repeat'); width relative to that of a reference structure ($rscale$); and the x -, z -, and azimuthal alignments (x , z , φ) of the origin. See also Fig. 3. The adjustment of the parameters to minimize the twofold phase residual (dashed box) is usually unnecessary, resulting in no changes to the parameters. Clearly there may be some advantage in repeating the overall procedure using the distortion-corrected structure as a new reference.

Each such whole repeat is first aligned approximately to the same twofold phase origin as the reference dataset, using standard methods [11]. It is then subjected to the automated sequence REFINE (Fig. 2, top right), which determines more accurately the values of the seven parameters, and also divides the whole repeat into sixths and determines for each $\frac{1}{6}$ -segment the values of ω , x , z , φ , and $rscale$. The x and z measurements from the $\frac{1}{6}$ -segments are used to calculate θ and 'repeat' for each $\frac{1}{3}$ -segment, and then SEARCH.COM (Fig. 2, bottom right) is run on the $\frac{1}{3}$ -segments to determine the other five parameters (ω , x , z , φ , and $rscale$). Finally, a full set of Fourier terms is extracted from the transform of each $\frac{1}{3}$ -segment and averaged with those from the other $\frac{1}{3}$ -segments to re-create the (now distortion-corrected) whole repeat.

The computations involved in accomplishing these steps are described in the following paragraphs.

3.4. Boxing and Fourier transformation

Areas of tube are boxed off from the densitometered arrays and Fourier transformed using the program HFTS. This program re-interpolates a selected length of tube (usually a whole repeat) at a specified rotation angle (θ) to make 4096 grid units, before boxing off a region 10% greater than the tube width, floating it (taking into account density gradients along the edges, in both x and y), and apodizing the edges; the boxed-off and re-interpolated area is then padded with zeros to make 2048 grid units width and Fourier transformed. HFTS also allows the whole repeat to be divided into any number of segments; the tube can be further rotated about the center of the selected segment by an angle $\Delta\theta$ and rescaled along its axis as though its effective repeat distance is $\text{repeat} \pm \Delta\text{repeat}$. Segments other than the one selected are collapsed to zero density and the Fourier transform is performed of the whole repeat (including the now-zero-density segments).

3.5. Refinement of axial repeats

Each whole repeat is aligned accurately to the reference dataset using the control program

REFINE. This program incorporates several automated sequences, described in more detail below. Initially, SEARCH.COM is run to determine the five parameters, ω , x , z , φ , and $rscale$. Next, REFINE iterates through ROTX.COM to determine the sixth parameter, θ , and through REPEAT.COM to determine the seventh parameter, 'repeat'. SEARCH.COM is then run again, and the sequence is continued until none of the parameters changes significantly.

SEARCH.COM begins by estimating just x and ω . This is done by comparing equivalent layer-line peaks on either side of the meridian in the transform and adjusting x and ω to minimize their phase asymmetry [26]. The Fourier terms lying within the first CTF zero are then extracted, using the x and ω estimates to correct the phases along the layer-lines, and an average is made of the terms from the near and far sides. z , φ , and $rscale$ are estimated next (to 0.01 Å, 0.01°, and 0.001 units precision, respectively) by minimizing the interparticle phase residual [27, 28] obtained by comparing the averaged Fourier terms with those of the reference dataset. x is then further refined (to 0.01 grid units precision) by minimizing the interparticle phase residual, this time with the Fourier terms from the near and far sides kept separate. If x changes significantly, SEARCH.COM iterates back, minimizing the phase asymmetry across the meridian to redetermine ω while keeping the new value of x . The new values of x and ω are used to re-extract the Fourier terms along the layer-lines, and then z , φ , $rscale$, and x are redetermined by minimizing the interparticle phase residual, as before. The iterations, and SEARCH.COM, end when x stops changing significantly.

ROTX.COM determines θ (0.01° precision) by minimizing the crystallographic R -factor calculated between the averaged Fourier terms and those of the reference dataset. REPEAT.COM determines the repeat distance, 'repeat' (1 Å precision), by maximizing the total amplitude on layer-lines beyond a specified distance (1/46 Å) up the meridian. Usually, many Fourier transforms need to be calculated before θ and 'repeat' converge to their best estimates, and 2048×2048 (rather than 2048×4096) arrays are used for these steps to reduce processing time.

3.6. $\frac{1}{3}$ -segments

Reliable estimates of θ and 'repeat' for the $\frac{1}{3}$ -segments could not be obtained by the same method as was used for the whole repeat. The more accurate and robust method devised was to subdivide each $\frac{1}{3}$ -segment into two halves, and to estimate θ and 'repeat' from the values of x , y , and z for each half. Determination of x and z for each half of the $\frac{1}{3}$ -segments is done by dividing the whole repeat into sixths, centered at evenly spaced y -locations, and running SEARCH.COM on each (therefore also determining ω , φ , and $rscale$).

An approximate value for the rotation angle of a $\frac{1}{3}$ -segment, θ_a , could be calculated from the x - and y -locations of its 'top' and 'bottom' halves:

$$\theta_a = \arctan\left(\frac{x_{\text{top}} - x_{\text{bottom}}}{y_{\text{top}} - y_{\text{bottom}}}\right). \quad (5)$$

In practice, however, the errors in x_{top} and x_{bottom} tended to be large (because they were obtained from very short segments: $\frac{1}{6}$ -segments), and a more accurate value of θ was obtained by averaging θ_a with the rotation angles estimated from neighboring top and bottom pairs of $\frac{1}{6}$ -segments.

The effective repeat distance of the $\frac{1}{3}$ -segment, 'repeat', is calculated similarly from the z -alignments of the origin for the 'top' and 'bottom' halves:

$$\text{repeat}_a = 6(z_{\text{top}} - z_{\text{bottom}}) + \text{repeat}_w, \quad (6)$$

with repeat_w representing the length of the whole repeat. Again, neighboring segments are averaged to improve accuracy.

Once θ and 'repeat' have been determined in this way for each $\frac{1}{3}$ -segment along the length of a tube, SEARCH.COM is run on each $\frac{1}{3}$ -segment to determine the other 5 parameters: x , ω , z , φ , and $rscale$ – and the complete three-dimensional alignment of each segment is thereby achieved.

3.7. Evaluation

Because of the presence of twofold axes oriented radially with respect to the tube axis, it was always possible to adjust the phase origin of a whole repeat so that the phases of all Fourier terms should be 0° or 180°. The data could therefore be assessed at this stage by averaging the $\frac{1}{3}$ -segments to make whole

repeats and calculating, from the whole repeats, twofold phase residuals:

$$\Phi_R = \frac{\sum F(R, l) \Delta\phi(R, l)}{\sum F(R, l)}, \quad (7)$$

where $\Delta\phi(R, l)$ is the phase deviation from the nearest of 0° or 180° , and $F(R, l)$ is the amplitude of the Fourier term, at radius R on layer-line l .

This twofold phase residual was also used as a basis for further refining the parameters if necessary (see Fig. 2, dashed box). The variations in the parameters along the length of the tube were plotted, including, for θ and 'repeat', alternative curves obtained from successive $\frac{1}{3}$ -segments and from successive $\frac{1}{6}$ -segments (see Fig. 7). Usually the discrepancies between the two sets of alternative curves were minor and could be neglected. In the few examples where this was not true, the parameter in question was adjusted and assumed to be improved if, as a result of the adjustment, Φ_R became smaller. Gross deviations in other parameters from one segment to the next were also checked in a similar manner.

3.8. Collection of higher resolution terms

The computations above to measure the distortions and align each $\frac{1}{3}$ -segment of a tube to the reference structure, were based on Fourier terms extending along the layer-lines only to the first zero of the CTF. Complete distortion-corrected datasets from both the near and far sides were required in the subsequent steps of CTF refinement, measurement of background noise, and merging of Fourier terms from different tubes. These datasets were obtained simply by extracting the Fourier terms from the transform of each (aligned) $\frac{1}{3}$ -segment of the tube out to the resolution cut-off (8 Å), and averaging them together.

3.9. Refinement of CTF

For each image, the defocus values along both the major and minor axes of astigmatism were refined by maximizing the agreement between the phases from the distortion-corrected dataset and the (already CTF-corrected) reference structure.

The near and far sides from each image were compared to the reference separately after their phases had been "corrected" for theoretical CTF variations, assuming in turn each of a set of defocus values within a narrow range about the original estimate. The best estimate was taken to be the defocus yielding the highest image Quality, Q_i , defined as the number of test phases in agreement with ($|\text{phase difference}| < 90^\circ$) the centrosymmetric reference phases, minus those opposed, divided by the total number of comparisons. Having obtained the best estimate from each side, the phases of the Fourier terms in its dataset were modified appropriately and an extra column was added to the dataset, listing the CTF value associated with each point. Defocus figures found by the refinement procedure were usually within ~ 500 Å of those estimated originally by sector-averaging of the amplitudes (see above), and consistent with the fact that the centers of mass of the two sides are approximately 400 Å apart.

Fig. 4 gives an example of the two-dimensional plots obtained by highlighting Fourier terms (from one side of a tube) whose phases agree (+) and disagree (–) with those of the reference structure. The overall quality, Q_i , was 0.30 for this side and 0.28 for the other side. By comparing the (+) with the (–) plots it was possible to get an idea of the general quality of the terms in different areas of the Fourier transform. Differences between the (+) and (–) plots always became difficult to distinguish by 10 Å resolution, indicating that the signal here was very weak. Values of Q_i for the different tubes ranged between 0.17 and 0.30, and for most tubes the near and the far sides gave similar results (mean difference: 0.02 ± 0.017 s.d.).

3.10. Measurement of background noise

Estimates of background noise were made from Fourier transforms of the ice on either side of the tube, using strips having the same dimensions as the portions of tube that had been boxed-off (see Fig. 6a). The Fourier transforms were added together incoherently, and the noise estimates were the amplitudes averaged locally about points at positions corresponding to the points along the layer-lines. These estimates were scaled so that

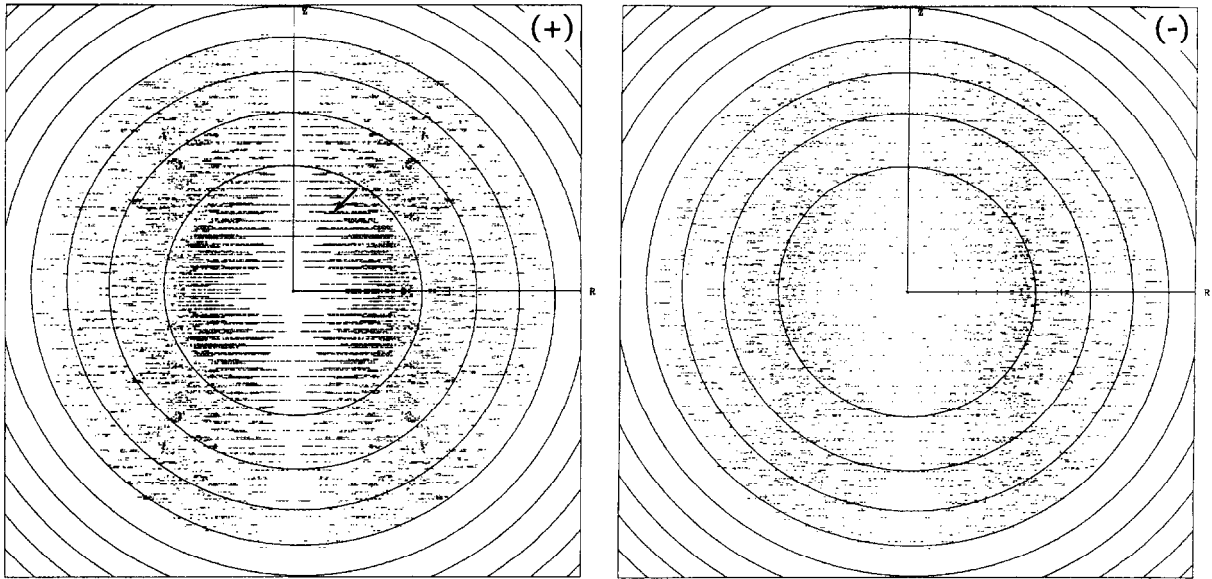


Fig. 4. Two-dimensional plots from the far side of a single (distortion-corrected) tube, highlighting those Fourier terms having the same ((+); left) and opposite ((-); right) phases to those from the reference structure. Concentric rings drawn over the plots indicate the positions of the zeros of the CTF (mean underfocus: 9900 Å). At low resolution, the (+) plot is stronger because the phases mostly agree with those of the reference, reflecting a good signal-to-noise ratio. At higher resolution, however, the difference between the two plots is harder to detect, reflecting a fall-off in signal-to-noise ratio. The CTF was refined by maximizing the number of terms in the (+) plot while minimizing the number of terms in the (-) plot. In both plots the unique Fourier terms were included together with their mirror-images across the meridian, giving the appearance of the Fourier transform of both sides of the tube. The arrow points to a layer-line ((0.5;30); [11]), at a resolution of $1/35 \text{ \AA}^{-1}$ (see also Fig. 6b); the plots extend to a resolution of $1/8.7 \text{ \AA}^{-1}$.

their sum equalled the sum of the layer-line amplitudes, and then incorporated as additional columns in the near- and far-side-CTF-corrected datasets. Thus each point along each layer-line was finally fully described in terms of its radial coordinate, amplitude, phase, CTF value and background noise.

3.11. Combining datasets

Datasets from the near and far sides of each tube were combined vectorially to make tube-averaged datasets and then the tube-averaged datasets were combined vectorially with each other to make the final dataset. In obtaining the tube-averaged datasets, the Fourier terms, $F_{ij}(R, l)$ (where i refers to the tube and j to the side), were weighted both by the image quality derived for the side, Q_{ij} , and by

the appropriate CTF value, $|T_{ij}(R, l)|$, as follows:

$$F_i(R, l) = \frac{\sum_j Q_{ij} |T_{ij}(R, l)| F_{ij}(R, l)}{\sum_j Q_{ij}}. \quad (8)$$

Background noise values, $BKG_{ij}(R, l)$, were squared before summing:

$$BKG_i(R, l)^2 = \frac{\sum_j (Q_{ij} |T_{ij}(R, l)| BKG_{ij}(R, l))^2}{(\sum_j Q_{ij})^2}. \quad (9)$$

The next steps were to reindex each tube-averaged dataset to be consistent with a single axial repeat (obeying the helical selection rule: $l = -81n + 253m$ ($n = 2n'$) [22]), and to remove regions of strong overlap (involving the first Bessel function peaks) that occurred between certain pairs of layer-lines, the precise pairs depending on the helical selection rule of the tube in question. The

tube-averaged datasets could then be combined, weighting the Fourier terms from each tube by its length:

$$F(R, l) = \sum_i L_i F_i(R, l), \quad (10)$$

and similarly for the associated background noise:

$$\text{BKG}(R, l)^2 = \sum_i L_i^2 \text{BKG}_i(R, l)^2. \quad (11)$$

The combined Fourier terms, corrected for the CTFs, were therefore

$$F_c(R, l) = \frac{F(R, l)}{\sum_{(i,j)} L_i T_{ij}(R, l)^2}. \quad (12)$$

We note that measurements of the combined terms were obtained at essentially all points out to the resolution limit, consistent with the helical symmetry of the tube. A small fraction of terms was usually excluded from individual datasets because of overlap of Bessel function peaks on certain pairs of layer-lines. However, the equivalent (non-overlap) terms would have been retained in other datasets, since different overlap patterns occur with tubes having different axial repeats. These differences between members of the same helical family arise because of very slight variations in dimensions of the p2 surface lattice [11].

3.12. PQ number

Finally, to identify those Fourier terms which should be discarded from the combined dataset because the signal is weak or absent, it was important to obtain an estimate of the signal-to-noise ratio at each point along each layer-line. Based on the individual figures for amplitude, F , phase, ϕ , and noise, BKG , we estimated the *point quality* as follows:

$$\text{PQ}(R, l) = \sqrt{\frac{2F(R, l)^2 \cos^2 \phi(R, l)}{\text{BKG}(R, l)^2}}. \quad (13)$$

To test how sensitively PQ measures the signal-to-noise ratio, it was useful to compare it to an alternative measure: $\cos^2 \phi$, which is 1 for terms in agreement with the centrosymmetric structure of the

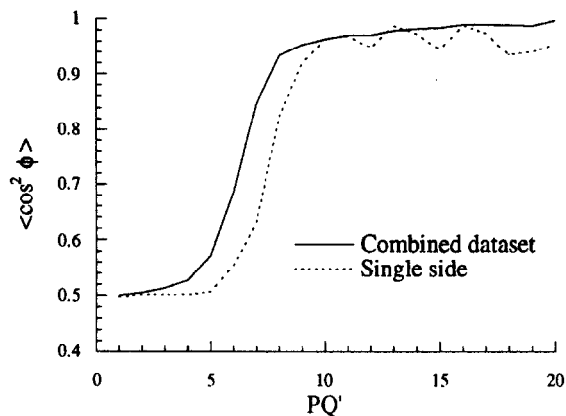


Fig. 5. Average value of $\cos^2 \phi$ for Fourier terms along the layer-lines plotted as a function of PQ' value. The continuous line represents all the terms from the combined dataset, and the dashed line all the terms from a single side of one tube. $\cos^2 \phi$ should be 1 for the centrosymmetric structure, but has an average value of 0.5 for random noise. Terms with high PQ' numbers have average $\cos^2 \phi$ values close to 1, while those with low PQ' numbers have average $\cos^2 \phi$ values closer to 0.5 – confirming that PQ' can be used as a measure of the signal-to-noise ratio. The continuous curve rises higher at lower PQ' values than the dashed curve does, showing that reduced errors in the estimates of the signal (F) and the noise (BKG) make the PQ' number a more sensitive indicator after the images have been combined. For the purpose of the graph, PQ' was calculated as $F/\sqrt{\text{BKG}^2}$, where F is the amplitude and BKG is the background noise level associated with the Fourier term. In practice, however, we take account of the phase as well: $\text{PQ} = \sqrt{(2F^2 \cos^2 \phi / \text{BKG}^2)}$, a more accurate measure of the signal-to-noise ratio than PQ' .

tube and 0.5 for random noise. Fig. 5 (continuous curve) plots the average values of $\cos^2 \phi$, taken from the combined dataset, for various modified PQ values (called PQ' , with the $\cos^2 \phi$ term in Eq. (13) removed so that the two estimates – PQ' and $\cos^2 \phi$ – are independent). The curve shows that $\cos^2 \phi$ averages 0.5 for terms with $\text{PQ}' \leq 1$ but rises to average 0.9 or higher for terms with $\text{PQ}' > 8$, indicating that PQ' is a sensitive indicator of signal-to-noise ratio¹. PQ' would therefore be an

¹ PQ' is similar to the q statistic used by Morgan et al. [20], but may be more reliable when small numbers of images are used because it takes advantage of an independent measurement of the background noise instead of one derived from the variation between measured amplitudes from different images.

appropriate measure for many specimens. However, the $F |\cos \phi|$ used in deriving PQ [Eq. (13)] is a more accurate measure of the signal from the ACh receptor tubes than the F used in deriving PQ' because $F |\cos \phi|$ disregards the imaginary components of the Fourier terms, which disagree with the known centrosymmetric structure of this particular specimen. With ACh receptor tubes, therefore, the PQ number provides the most sensitive means of distinguishing between Fourier terms with high and low signal-to-noise ratio, taking account of their strength relative to the background noise and also their phase.

Ultimately, errors inherent in the PQ measurements limit the ability to filter the good terms from the noisy ones. The errors decrease as more images are combined, since the estimates of signal and of background noise then become more reliable. The dashed curve in Fig. 5, representing the data from a single side of one tube, falls below the plot from the combined dataset because many terms having a low signal-to-noise ratio have been 'mistakenly' assigned high PQ' numbers. As a result, the slope of the curve is almost flat in the region where $\cos^2 \phi$ averages 0.5, confirming that PQ' numbers from a single image are less sensitive in discriminating the signal from noise.

3.13. Calculation of the structure

Fourier terms, F_c , having PQ numbers below 1.7 were considered to be too close to the noise level to have any significance and were discarded from the final set of structure factor terms, which extended to a resolution of 8 Å. A small fraction of additional terms were discarded, where the PQ number, averaged locally, was small. These terms were considered inconsistent with the continuous nature of the Bessel modulations along the layer-lines. A total of 10 536 terms on 330 layer-lines remained, yielding an overall two-fold phase residual, Φ_R , of 8.6°. The real components of the remaining terms were incorporated in a Fourier–Bessel inversion to derive the helical density waves as a function of radius, and a three-dimensional map in sections parallel and perpendicular to the tube axis was calculated from the densities by Fourier synthesis in the standard way [26, 29].

4. Results

An example of an image of an ACh receptor tube is shown in Fig. 6a. Individual receptors consist of five homologous membrane-spanning subunits (molecular masses: 50–60 kD) arranged symmetrically around a central axis, which delineates the pathway for the ions. Depending on the defocus conditions and the local pattern of overlap, the receptors may appear as rosettes when viewed down this axis (central portion of the tube) or give rise to striations when viewed from their sides (edges of the tube). The striations (apparent in Fig. 6a) arise mainly from the extracellular ends of the receptors, which protrude radially outwards from the membrane surface.

The distortion corrections were carried out on 28 images of ACh receptor tubes, 26 of which had been analyzed previously by dividing the tubes into whole repeats, i.e. without any such corrections being applied [22]. The tubes were selected on the basis of their straightness, uniformity in appearance, and the quality of their diffraction patterns (Fig. 6b). As described in Methods, lengths of tube consisting of whole axial repeats were first subdivided into thirds: i.e. into segments on average about as long as they were wide. Each $\frac{1}{3}$ -segment (total 225) was then fully aligned in three dimensions against the reference structure by determining the set of seven parameters: ω , θ , repeat, x , z , ϕ , and r scale (Figs. 2 and 3). Finally, the Fourier terms from each aligned $\frac{1}{3}$ -segment were extracted to a resolution of 8 Å and combined with the others to make a distortion-corrected dataset, which was used to calculate a three-dimensional map.

4.1. Path of tube through the ice

Fig. 7 shows a typical set of curves plotting the variations in x , rotation angle (θ), out-of-plane tilt (ω), repeat, and r scale. They were obtained from successive $\frac{1}{3}$ -segments along the tube in Fig. 6a (alternative curves for θ and 'repeat', calculated from $\frac{1}{6}$ -segments, are also shown in Fig. 7b and Fig. 7d). This tube is slightly bent, as can be seen from the cup-shaped curve made by the displacements in the x -direction (Fig. 7a) and the corresponding changes in the rotation angle as a function

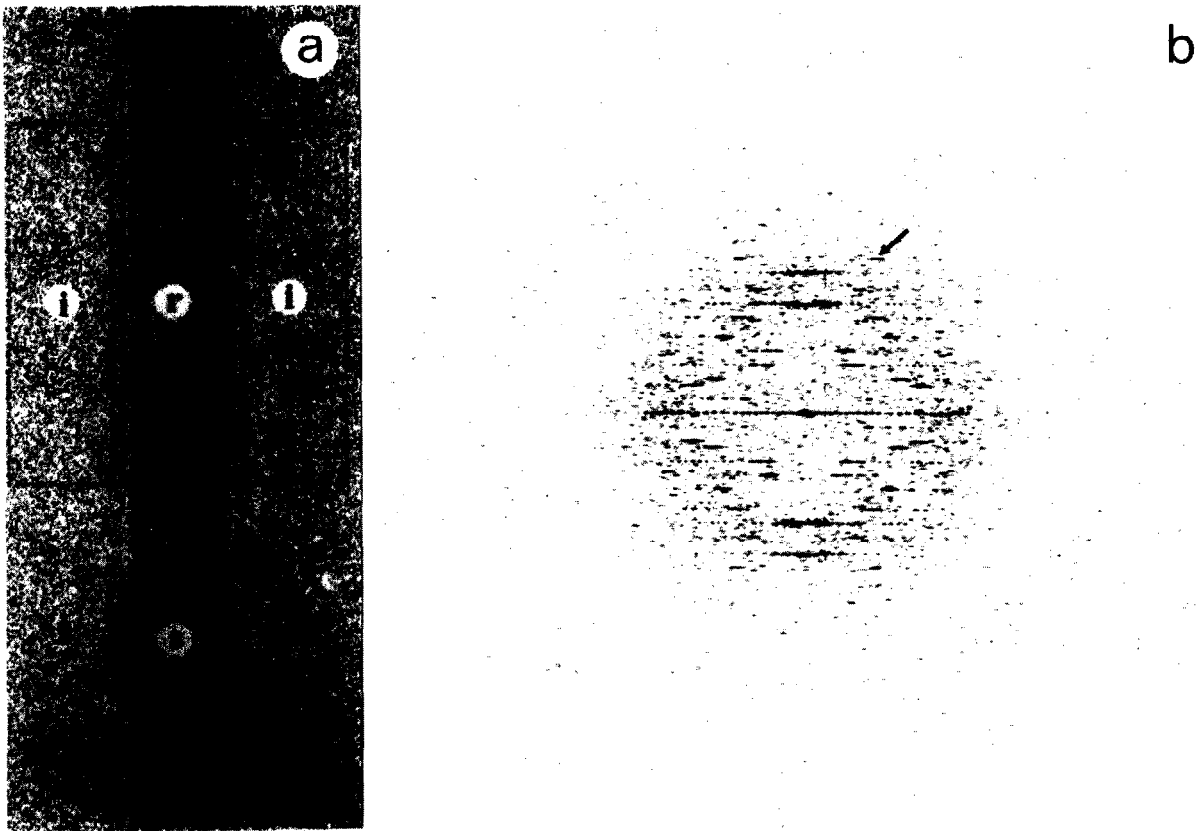


Fig. 6. ACh receptor tube embedded in amorphous ice and imaged at $10\,400\text{ \AA}$ underfocus: (a) scanned image; (b) computed Fourier transform of the boxed-off area. *r*. In (a), the boxes labeled *r*, *s* and *i* enclose, respectively, a whole axial repeat, a $\frac{1}{3}$ -segment, and repeat-long-tube-wide strips of ice on either side of the tube; the variations along this tube, due to different types of distortions, are plotted in Fig. 7; (b) shows a mirror-symmetric pattern of layer-lines that extend clearly only to a resolution of $\sim 1/35\text{ \AA}^{-1}$ (arrow) before the distortion corrections have been applied (but much further afterwards; see Fig. 4); the Fourier transforms summed from several areas equivalent to *r* and *i* were used to estimate, respectively, the CTF variations and background noise (see Section 3). Scale bar in (a) corresponds to 500 \AA .

of tube length (Fig. 7b). The two curves in each of Fig. 7b and Fig. 7d, representing alternative estimates of θ and 'repeat', respectively (see Section 3), are in good agreement with each other, as expected if the measurement inaccuracies are small. Other distortions present include variations in tilt, especially towards one end of the tube ($y > 9000\text{ \AA}$; Fig. 7c), and an approximately linear shortening of the repeat distance at the other end (Fig. 7d). The radial dimensions of the tube also change by $\sim 2\%$, making it about 15 \AA narrower at one end than the other (Fig. 7e).

The more substantial changes in Figs. 7b–Fig. 7d are predominantly linear, consistent with the theoretical descriptions of the distortions given above. However fluctuations on a finer scale are also apparent. These are most likely caused by higher order distortions than the ones we assumed, or by localized disturbances (in either case causing less signal loss than the assumed distortions). They are unlikely to represent measurement inaccuracies, since these have smaller effects (see below). Even shorter-range distortions are undoubtedly present, but not seen because they are localized within the

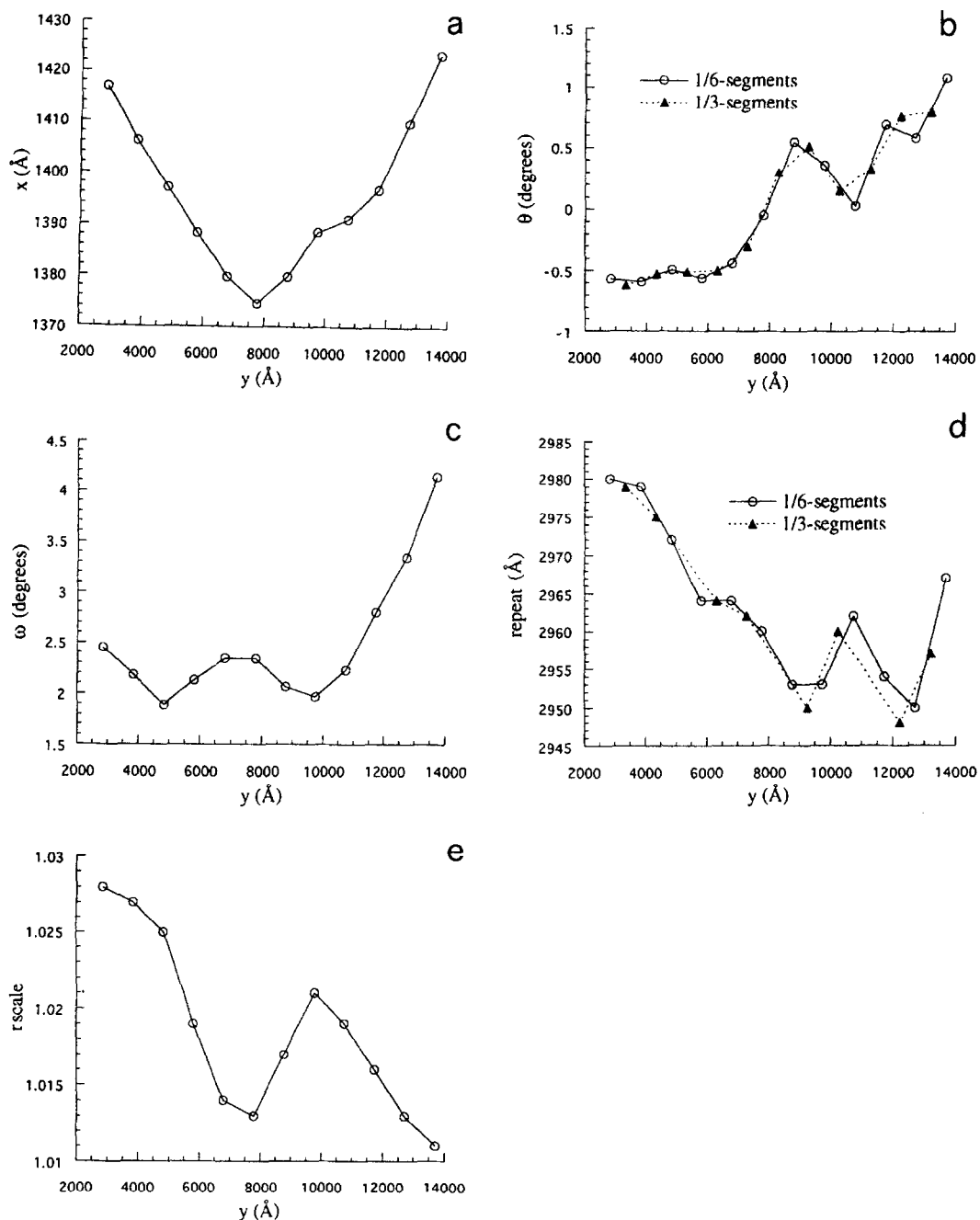


Fig. 7. Variations in: (a) x -position; (b) rotation (θ); (c) tilt (ω); (d) 'repeat'; and (e) r scale plotted along the length of the tube shown in Fig. 6. Each circled point represents the value of the appropriate parameter at the center of a segment a third of the length of the whole axial repeat. The tube was composed of four whole repeats; hence twelve $\frac{1}{3}$ -segments are represented. The values of θ and 'repeat' at the center of each $\frac{1}{3}$ -segment were calculated from the x - and z -locations of its top and bottom halves, after dividing the whole repeat into six parts (see Section 3). Values of θ and 'repeat' at the midway positions were also calculated from the x - and z -locations of the successive $\frac{1}{3}$ -segments (filled triangles; broken curves).

$\frac{1}{3}$ -segments. Since they extend over such short lengths, however, they are unlikely to result in significant displacements or signal loss, even if they are not taken into account (see Section 1).

4.2. Magnitude of distortions

The tubes were usually not visibly distorted, except perhaps for slight bending or changes in tilt (indicated by the changing pattern of striations at their edges). Yet the alignments of their $\frac{1}{3}$ -segments to the reference structure differed consistently, by amounts too small to be visible, when comparing successive segments along the tubes (Table 1). The x - and z -alignments of the segments (from which θ and 'repeat' are calculated) differed, on average, by about 1 Å; their tilts and twists differed, on average, by about 0.3° (corresponding to displacements of ~ 1.5 Å); and their widths differed, on average, by about 0.8%.

Furthermore, the segment-to-segment variations were in many instances greater than the amounts suggested by the tabulated figures. For example, whereas about half of the successive $\frac{1}{3}$ -segments differed in their x -locations by less than 1.3 Å (the median value listed in Table 1), about one in eight differed by 4 Å (the median plus standard deviation) or more. Also, tubes yielding small differences in one parameter often yielded large differences in another. These departures from the average properties are of particular concern, since larger displacements have a disproportionately greater effect.

4.3. Measurement inaccuracies

To assess the errors involved in measuring each type of distortion, we took the distortion-corrected datasets derived from three tubes (11 whole repeats) and divided each of them into two half-datasets made up from alternating points along the layer-lines. The five primary alignment parameters: x , z , ω , φ and r_{scale} (as in Table 1) were then determined separately from each half-dataset, and the values obtained for equivalent whole repeats and $\frac{1}{3}$ -segments were compared. Table 2 lists, for each parameter, the median differences, the standard deviations and the maximum differences found between the two half-datasets.

A notable result indicated by the table is that the errors associated with measurements from the $\frac{1}{3}$ -segments are similar to those from the whole repeats. For most of the parameters, the measurement errors only increase marginally as the segment size is reduced. The estimates for the z -locations in fact appear to become more accurate as the segment becomes shorter. The lack of improvement of measurement accuracy with increased tube length should not be surprising, however, since the parameters vary by greater amounts over longer lengths of tube, counteracting the potentially greater amount of signal used in their measurement. Different short segments of an unevenly stretched tube, for example, would yield different values for the repeat, and the signal dominating the estimate for the whole repeat might come from only one of these short segments.

Table 1
Magnitude of distortions: differences between successive $\frac{1}{3}$ -segments

	x (Å) ^a	z (Å)	ω (deg)	φ (deg) ^b	r_{scale} ^c
Median	1.3	0.9	0.28	0.29	0.008
S.D. ^d	2.7	1.1	0.24	0.31	0.008
Range	0.0–24.3	0.0–8.3	0.0–1.11	0.0–1.99	0.003–0.032

^aAll the figures shown were calculated after each whole repeat had been aligned to the reference structure.

^b0.1° \approx 0.5 Å, at the radius of the membrane.

^cDifferences in r_{scale} between the widest and narrowest segments of each tube.

^dStandard deviation from the mean of the 150 measurements (28 in the case of r_{scale}).

Table 2

Measurement inaccuracies: differences between parameters determined using different halves of the dataset

		x (Å)	z (Å)	ω (deg)	φ (deg)	r_{scale}
Whole repeat $\frac{1}{3}$ segment	Median	0.21	0.26	0.05	0.02	0.002
	S.D. ^a	0.16	0.15	0.03	0.02	0.001
	Maximum observed	0.66	0.45	0.12	0.07	0.003
	Median	0.29	0.10	0.07	0.04	0.002
	S.D. ^a	0.24	0.13	0.11	0.03	0.002
	Maximum observed	1.07	0.52	0.37	0.12	0.007

^aStandard deviation from the mean of 11 (whole repeat) or 33 ($\frac{1}{3}$ -segment) measurements.

Comparing the figures obtained for the $\frac{1}{3}$ -segments in Table 2 with those obtained in Table 1, we find that the measurement errors are small in comparison with the displacements caused by the distortions, and therefore the differences between successive segments listed in Table 1 represent distortions, not measurement inaccuracy.²

4.4. Evaluation of single images

The qualities of the datasets from single images could only be evaluated reliably using Fourier terms out to the first CTF zero (typically $\sim \frac{1}{15} \text{Å}^{-1}$), because of the poor signal-to-noise ratio at higher resolution. Within this cut-off, every one of the distortion-corrected datasets yielded a two-fold phase residual, Φ_R , better than that of the corresponding uncorrected dataset. The range of improvement was 0.14° – 5.19° , and the average residual was 28.4° before correction and 27.0° afterwards (compared to 45° for random data). This represents a gain in signal retention of 9%, deter-

mined by calculating the signal-to-noise ratio in terms of Φ_R :

$$S/N = \frac{\sqrt{\cos^2 \Phi_R - \sin^2 \Phi_R}}{\sqrt{2} \sin \Phi_R} \quad (14)$$

Calculations using appropriate values in Eq. (4) suggest that this gain is about the amount one would expect at 20 Å resolution, where much of the low-resolution data lies, if the maximum displacements produced by second-order distortions were reduced by the corrections from $\sim 2.9 \text{Å}$ to $\sim 0.3 \text{Å}$. One can calculate further that the same corrections, at $\sim 10 \text{Å}$ resolution, should lead to an improvement in the signal retention from 72% to 100%, i.e. a gain of 38%. While the poor signal-to-noise ratios associated with single images makes it impossible to measure their gains at $\sim 10 \text{Å}$ resolution, such measurements can be made after the images have been combined and do in fact show a gain of $\sim 40\%$ (see below).

4.5. Improvements in the combined dataset

Table 3 lists the average amplitudes and signal-to-noise ratios of the Fourier terms obtained from the combined dataset, before and after correcting the distortions. The results are shown for annuli at successively higher resolution, with the data being divided into separate Z - and R -sectors to reveal any significant differences parallel and perpendicular to the axis of the tube. To ensure a valid

² We can divide the values in Table 1 into two components: a “real” component, reflecting distortions, and a component due to measurement inaccuracy. The “real” component is equal to: $\Delta_{\text{real}} = \sqrt{\Delta_{\text{parameter}}^2 - 2\text{m.i.}^2}$, where $\Delta_{\text{parameter}}$ is the value in Table 1 and m.i. is the measurement inaccuracy for the $\frac{1}{3}$ -segments, from Table 2. Using typical values for each, Δ_{real} turns out to be approximately equal to $\Delta_{\text{parameter}}$ for all the parameters listed, indicating that the errors of measurement can be neglected.

Table 3
Statistics of combined dataset before and after distortion correction

Resolution range (Å)	Z-sector				R-sector				Gain ^d
	Published ^a		Corrected		Published		Corrected		
	$ F_{\text{avg}} ^b$	S/N ^c	$ F_{\text{avg}} $	S/N	$ F_{\text{avg}} $	S/N	$ F_{\text{avg}} $	S/N	
46–23	27.2	2.89	27.0	3.06	13.9	2.29	14.1	2.41	5%
23–15	5.4	1.39	6.1	1.56	3.5	0.78	4.1	0.97	17%
15–11	2.3	0.72	2.7	0.93	2.1	0.46	2.1	0.57	29%
11–9	1.7	0.36	1.8	0.43	1.9	0.08	1.8	0.15	37%

^aFrom Ref. [22].

^bAverage amplitudes of Fourier terms in annuli at successively higher resolution. All possible Fourier terms are included in each annulus.

^cAverage signal-to-noise ratios of the Fourier terms calculated as follows:

$$S/N = \frac{\sqrt{2Q'}}{\sqrt{1-Q'}}$$

where

$Q' = \frac{\sum_{(R,\theta)} F(\cos^2 \phi - \sin^2 \phi)}{\sum_{(R,\theta)} F}$ and the summations range over all layer-line terms in the given annulus and sector. The signal-to-noise ratio should be ∞ for pure signal and 0 for pure noise. In calculating the three-dimensional map, many terms were eliminated because they were below the PQ threshold (see Section 3).

^dGain, due to distortion corrections, in the average signal-to-noise ratio.

comparison, both datasets contain all possible Fourier terms, including those that would be discarded later due to low PQ numbers.

The comparison of the signal-to-noise ratios shows that the distortion corrections have brought about roughly equal improvements in both sectors. Moreover, the improvements have become greater with increasing resolution, as indicated by the slightly higher amplitudes (mainly in the Z-sector) in the higher resolution ranges, and by the percentage gains (final column) in the signal retention over the noise. At 20 Å resolution the gain is in the region of 10%, or a similar figure to the average 9% gain exhibited by the single images. However by 10 Å resolution (range: 11–9 Å), the signal-to-noise ratios have improved by almost 40%, which is close to the figure calculated above assuming the distortions are predominantly second-order effects.

4.6. Three-dimensional map

The three-dimensional map was calculated as described in Section 3, using PQ numbers to select Fourier terms having significant signal-to-noise ra-

tios. Features of secondary structure described previously [22] are more clearly resolved as a result of the distortion corrections, and are more accurate, as judged by improvements in five-fold symmetry at several levels in the receptor. Fig. 8a gives an example of the details seen in a section normal to the pseudo-five-fold axis of the receptor at a tube radius of 338 Å, i.e. at a level ~ 30 Å from the membrane surface, before the distortion corrections had been applied. The locations of the two α subunits (α_δ and α_γ) and a neighboring δ subunit are indicated [30]. Each subunit at this level is thought to contain three short α -helices running approximately normal to the membrane and which accordingly appear as three peaks of density (denoted I, II, and III for α_δ). These peaks are not expected to have identical features in comparing one subunit with another around the ring, because the two α subunits have different conformations [31], and the remaining (β , γ , and δ) subunits have only 36–41% amino acid identity to the α subunit. Nevertheless, the degree of equivalence of the subunits and the resolution of the three peaks should improve as the signal-to-noise ratio gets better.

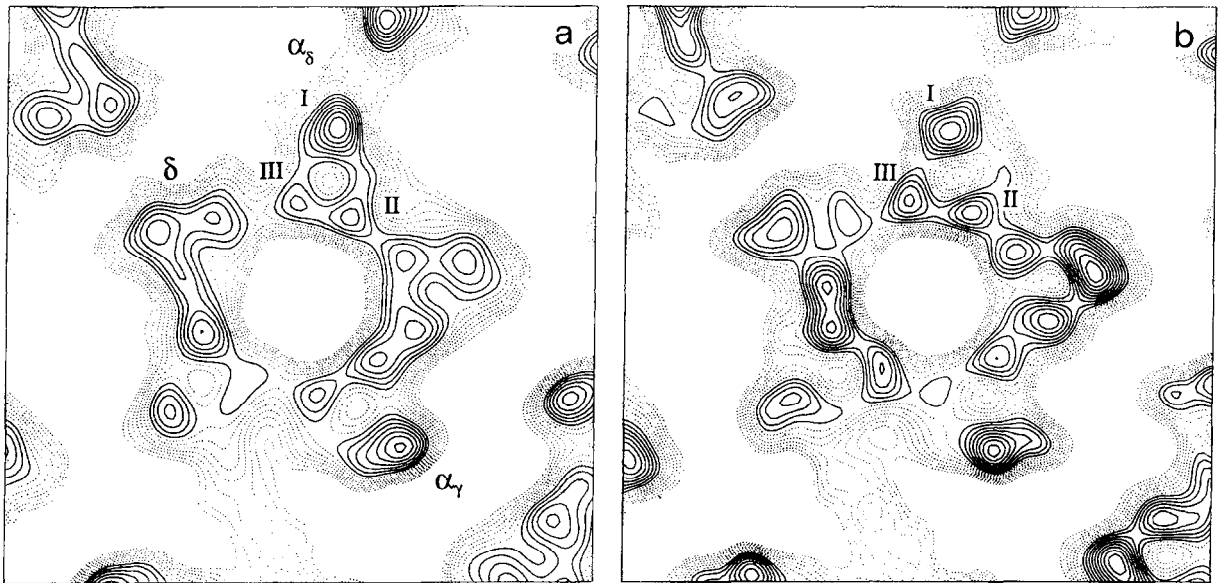


Fig. 8. Sections normal to the pseudo-five-fold axis of the receptor, through the putative ACh binding sites: (a) from the published structure [22], and (b) from the structure determined after correcting distortions. The five subunits together form a ring of density encircling a central pathway for the ions. At this level, three (α -helical) rods are present in each subunit, running approximately parallel to the pseudo-five-fold axis. In the sections, these rods give rise to three peaks of density (I, II, and III) surrounding a central depression. Almost all the peaks (continuous contours) are better resolved after distortion correction, and the improvements appear to take place approximately equally in the directions parallel to (vertical) and perpendicular to the tube axis. The subunit assignments (α_γ , α_δ , δ) are based on electron crystallographic labeling studies [24, 30]. The vertical dimension of the sections corresponds to 108 Å.

Fig. 8b, which is of the same section after the distortion corrections have been applied, demonstrates that major improvements are indeed achieved. Almost all of the peaks have become better resolved as a result of the distortion corrections, enhancing the similarities in appearance of the different subunits. Particularly noticeable is the change in appearance of the δ subunit, which has only one clearly marked peak before the distortion corrections have been applied (Fig. 8a), but has become more like the other subunits afterwards (Fig. 8b). The new features must reflect the actual structure, since the distortion corrections do not bias the δ subunit towards looking like the other subunits or being composed of three peaks.

The peaks of density in Fig. 8 are separated from each other by ~ 10 – 14 Å, so the improvement in resolving them must be due to increased signal at high resolution. Notably, the improvement has been achieved without any enhancement of the

high-resolution terms by applying a temperature factor weighting.

5. Discussion

Arrays of biological molecules suitable for analysis by electron microscopy rarely, if ever, align themselves on a perfect crystal lattice over very long distances. For various reasons, the arrays contain long-range disturbances, or distortions, which need to be measured accurately and corrected before the structure of an average molecule can be determined to the highest possible resolution. With two-dimensional crystals, bending in the plane of the array is usually a significant distortion, and corrections for this effect have led to substantial gains in the signal retrieved [8]. With tubular crystals, gross amounts of bending have also been corrected [3], giving rise to improvements, but only at

low resolution. In the present study, we have examined other kinds of distortions in tubular crystals, in addition to bending, with a view to establishing a general correction procedure that will ultimately allow atomic resolution to be achieved.

5.1. Segment-by-segment correction

The method we used to measure and to correct the distortions was to divide the tubes into short segments, align each segment in three dimensions to a reference structure, and then add the segments together after the misalignments had been removed. Seven parameters had to be defined to describe completely the alignment of each segment in three dimensions, and an iterative procedure (Fig. 2) was developed to determine them with the highest possible accuracy. In applying the procedure to the ACh receptor tubes, we showed that all of the parameters could be measured with an accuracy sufficient to plot reliably their variations along the length of the tube (Fig. 7). The three-dimensional map of the ACh receptor, obtained after taking these variations into account, revealed more clearly elements of secondary structure and showed a greater degree of equivalence between neighboring subunits (Fig. 8), as expected from the improvements in the signal-to-noise ratio. Importantly, the extent in resolution of 8 Å after applying the corrections appears to derive mainly from the small number of images and their limited quality. The method itself seems to have recovered almost all of the signal loss due to distortions to a resolution well beyond 8 Å, as discussed below.

In correcting distortions by complete three-dimensional alignment, segment-by-segment, we take advantage of the fact that tubular crystals contain an appreciable amount of information per unit length, and make optimal use of the symmetry present. Only features consistent with the inherent helical symmetry are reinforced when the information from many different tubes are averaged, whereas any non-helical features present become weaker in the same sense as would, e.g., statistical noise. Furthermore, most of the manipulations are done in reciprocal space, which is an advantage in terms of simplicity and the speed with which the para-

meters can be refined, and in terms of facilitating direct assessments of the errors involved.

The actual procedures devised were such that measurement inaccuracies would be mostly due to random, rather than systematic errors, and compensatory in going from one segment to the next. They should also apply if, for example, a tube has been judged to have a different axial repeat than one that is strictly correct. By dividing the tube into short segments and independently aligning each segment (particularly its position along and azimuthally around the axis), the tube would be recentered before the displacements due to the use of an incorrect repeat became large. Therefore, the errors incurred and consequent signal losses would be minimal.

5.2. Signal gains at high resolution

While the signal losses caused by the distortions were minor at low resolution, they increased rapidly as a function of resolution, so that correcting them resulted in an almost 40% gain in the signal-to-noise ratio near the 9 Å limit (Table 3). The ability to correct distortions, and so retain the signal, will therefore be critical in any attempt to extend the structural analysis to even higher resolutions. If the same approach is to be taken as we have described, it will be important that the losses due to the residual distortions within the $\frac{1}{3}$ -segments (which remain uncorrected) remain small, and that any increased losses associated with extra errors in aligning the $\frac{1}{3}$ -segments (rather than whole repeats) do not begin to outweigh the gains made by fitting the distortions more closely.

Table 4 gives estimates of the distortion-induced signal losses that would be incurred in whole repeats and in $\frac{1}{3}$ segments at a resolution of 5 Å by the different kinds of distortion and alignment errors, based on their observed magnitudes (Tables 1 and 2) and the equations in the Appendix. The “typical” values shown are those associated with the median displacements in Table 1, whereas the “strong” values are those associated with displacements equal to the median plus the standard deviation. Signal losses accompanying two-dimensional distortions (bending and scale changes) cause equal signal loss in all Fourier terms at a particular

Table 4
Estimates of % signal loss^a at 5 Å resolution due to different types of distortion

		Bend θ	Stretch 'repeat'	Tilt ^b ω	Twist ^c φ	Flattening <i>r</i> scale
Whole repeat	Typical ^d	72	47	92	82	3
	Strong ^e	86	79	122 ^f	83	11
$\frac{1}{3}$ segment	Typical	2	1	15	3	3
	Strong	15	4	32	12	11

^aIn the direction of maximum displacement.

^bBessel order = 10, $Z = 0.2 \text{ \AA}$, $X = 0.005 \text{ \AA}^{-1}$ (beginning of a near-meridional layer-line).

^cBessel order = 430.

^dDue to a distortion of median magnitude.

^eDue to a distortion of large magnitude (median plus standard deviation).

^fFourier amplitudes have the wrong sign and 22% of the correct magnitude.

resolution in the direction of displacement, making the figures for these distortions readily appreciated. However, signal losses accompanying three-dimensional distortions (variable tilt and twist) depend on other factors as well, including the Bessel order, n , of the Fourier term and (in the case of tilt) the location of the term in reciprocal space; the major losses here tend to be confined to a relatively smaller proportion of the data. Bearing in mind these limitations in comparing the different estimates, the table suggests that the three- and the two-dimensional distortions would contribute roughly equally to loss of signal at 5 Å resolution, and that whereas each of the four major distortions is likely to cause unacceptable signal loss if left uncorrected (i.e. tubes analyzed as whole repeats), acceptable losses (in general, < 15%) should be achievable if corrections are applied by dividing the repeats into $\frac{1}{3}$ -segments.

Flattening of the tubes in the direction parallel to the electron beam is the only potentially serious distortion that cannot be corrected straightforwardly by alignment of short segments. However, the signal losses due to flattening appear negligible anyway in the tubes we have selected (Table 4). We also found that the variations in *r*scale along the length of the tube were very small (Table 1), and the differences in image quality, Q_i , between the near and far sides were, on average, less than 10%. These observations suggest that flattening (or uneven compression of the two sides) was not a significant effect, and hence this type of distortion can largely be avoided by applying stringent selection criteria.

In Table 5, we estimate the effect of measurement inaccuracies on the signal losses at 5 Å resolution, in a similar way as was done for the distortions, using the observed values for the different types of inaccuracies given in Table 2. As was the case with the distortion estimates, signal losses due to inaccuracies in measurement of the two-dimensional parameters depend only on resolution in the direction of the inaccuracy, whereas the losses due to inaccuracies in measurement of the three-dimensional parameters depend on additional factors. The Table suggests that the signal losses accompanying the measurements would all be relatively minor when whole repeats are analyzed, and that the losses would be mostly higher, but still minor, when the repeats are divided into $\frac{1}{3}$ -segments. The only case where the inaccuracies could become serious, after dividing the repeats into $\frac{1}{3}$ -segments, are in the measurement of tilt. However the large inaccuracies in tilt were rare, and the extreme losses listed in the Table are restricted to a small region of the Fourier transform even in those rare cases.

5.3. Properties of distortions in tubular crystals

The ACh receptor tubes were ideal specimens for the distortion analysis since they had already been well characterized in earlier studies without any distortion corrections being applied [11, 12, 23]. One property of these tubes revealed by the present study was that the three-dimensional distortions, variations in out-of-plane tilt and twist, resulted in

Table 5
Estimates of % signal loss at 5 Å resolution due to measurement inaccuracies

		Bend ^a θ	Stretch ^b 'repeat'	Tilt ^c ω	Twist ^d φ
Whole	Typical ^e	3	5	6	1
repeat	Strong ^f	11	13	15	4
$\frac{1}{3}$ segment	Typical	7	1	12	4
	Strong	21	4	68	13

^aEstimated from errors in x -location, Table 2.

^bEstimated from errors in z -location, Table 2.

^cBessel order = 10, $Z = 0.2$ Å, $X = 0.005$ Å⁻¹.

^dBessel order = 430.

^eDue to an inaccuracy of median magnitude.

^fDue to an inaccuracy of large magnitude (median plus standard deviation).

displacements that were comparable in magnitude to the displacements caused by the two-dimensional distortions, bending and changes in scale (Fig. 7; Table 1). Another property was that these different kinds of distortion each individually were often strong enough to cause appreciable signal loss.

That no particular distortion had a dominating effect may to some extent have reflected our selection criteria, in which the diffraction patterns of the tubes were required to be mirror-symmetric and appearing equal in quality in all directions. But it also seems likely that the properties we observed are general for specimens of this type. Because of the cylindrical symmetry and the freedom of movement in the ice, flexibility in one sense is probably associated with flexibility in another. Hence if the tubular crystals being analyzed bend readily, as one can observe directly from the micrographs, they almost certainly vary substantially in tilt and twist as well. This argument adds weight to the conclusion above that it is important, in correcting distortions in tubular crystals, to take account of the three-dimensional distortions at the same time as the (more obvious) two-dimensional ones.

5.4. Prospects

The figures in Tables 4 and 5 suggest that the improved fitting to the reference structure achieved by dividing whole repeats into thirds results in signal gains which will continue to outweigh the losses due to measurement errors until a resolution

well beyond 5 Å is reached. Assuming the maximum displacements due to the distortions are reduced from 2.9 Å to 0.3 Å by the corrections (see Section 4), it can be shown that at 3.5 Å resolution only ~ 3% of the signal should be lost to distortions, while the gain relative to the signal from a whole repeat should be ~ 400%. The distortion correction procedure described should therefore provide an appropriate way to extend the structural analysis of tubular crystals, such as we have examined, to atomic resolution.

The attainment of this resolution would, however, require much better images than the standard 120 kV images used here. Pilot experiments have been conducted with a 400 kV instrument and with a 300 kV field emission instrument incorporating a liquid-helium cooled stage, to determine the relative effects of better electron optics, reduction in multiple scattering and the additional protection from radiation damage at liquid helium temperatures. Images recorded with the latter instrument (A. Miyazawa, Y. Fujiyoshi, R.B. and N.U., unpublished) have indeed yielded higher signal-to-noise ratios (average Q_i : 0.30 ($n = 10$), compared with 0.24 ($n = 26$) from the 120 kV images), indicating that major improvements in the microscopy are possible.

6. Conclusion

A procedure has been developed for correcting distortions in tubular crystals which independently

aligns short tube segments against a reference structure, allowing correction of distortions in all three dimensions while maintaining high accuracy in their alignment. Application of the procedure to ice-embedded ACh receptor tubes shows that:

(a) The three-dimensional distortions (variations in out-of-plane tilt and twist) and two-dimensional distortions (bending and scale changes) are about equally important.

(b) Division of the tubes into segments about equal to their widths allows retention of almost all of the available signal, reducing the losses due to distortions from high levels without significantly increasing the signal losses due to increased inaccuracy in the alignments.

(c) The corrections improve the signal-to-noise ratios of the Fourier terms from single tubes, and from the combined data, by $\sim 10\%$ at low resolution (20 Å). This improvement increases steadily to $\sim 40\%$ by 9 Å resolution.

(d) The finer structural details are more clearly resolved as a result of these improvements, and extrapolations suggest that much greater gains in signal retention should be achieved when better images become available.

Acknowledgements

We are very grateful to Drs. R.A. Crowther, R. Henderson and C. Toyoshima for helpful discussions. Drs. K. Downing and R.M. Glaeser (Berkeley, California, USA) and Dr. Y. Fujiyoshi (Kyoto, Japan) kindly allowed us to record images with their high voltage electron microscopes for some of this work. The *T. marmorata*, from which the tubular crystals were obtained, were supplied by the Marine Station, Roscoff, France. The research was supported in part by a Glaxo Dorothy Hodgkin Scholarship (to R.B.) and a grant from the National Institutes of Health (GM41449).

Appendix A

This section describes some of the more common types of distortions in tubular crystals and derives formulae for the signal losses they would incur. The

tube is considered to be in the xy plane, with the y axis parallel to the tube axis at the origin. With purely two-dimensional distortions (e.g. bend, shear, or stretch), the positions (x', y') of each point in the distorted tube are related to the positions (x, y) of that element in the undistorted tube by some rule of transformation – the rule describes the distortion (Fig. 9). Three-dimensional distortions like tilt and twist can often be described more readily by examining their effects on the phases in reciprocal space.

A.1. Bend in the image plane

If the axis of the tube follows the path of a circle of radius R_c , then the location of every point in the tube can be described by

$$(x' - R_c)^2 + y'^2 = (x - R_c)^2, \quad (\text{A.1})$$

$$y' = (x - R_c) \sin\left(\frac{y}{x - R_c}\right), \quad (\text{A.2})$$

$$x' = (x - R_c) \cos\left(\frac{y}{x - R_c}\right) + R_c. \quad (\text{A.3})$$

Tubes which are strongly bent are never analyzed. For tubes with a small amount of bend, R_c is much greater than both x and y , so the above equations

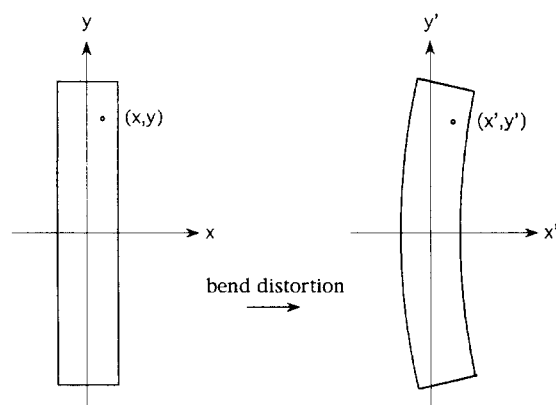


Fig. 9. Relation between an undistorted tube (left) and a distorted one (right). Each point (x, y) in the undistorted tube is moved by the distortion (bend in this case) to the point (x', y') . The relation between (x', y') and (x, y) is the transformation rule of the distortion.

can be simplified:

$$y' = y \tag{A.4}$$

$$x' - x = \Delta x = R_c \left(1 - \cos \frac{y}{R_c} \right). \tag{A.5}$$

Expanding the cosine into a power series and taking only the first term,

$$\Delta x = \frac{y^2}{2 R_c}, \tag{A.6}$$

showing this to approximate a second-order distortion (see above). The displacement, Δx , is wholly in the x direction, giving the greatest signal losses for Fourier terms far from the meridian (large X). Fig. 1a shows the signal loss as a function of segment length for a second-order distortion like bend.

A.2. Stretch along the tube axis

A linear stretch:

$$y' = by \tag{A.7}$$

is not a distortion; it is a misalignment of the repeat distance, which is the parameter describing the axial scaling of the tube (see Section 3). A second-order stretch:

$$y' = y + b \operatorname{sgn}(y) y^2, \tag{A.8}$$

where $\operatorname{sgn}(y)$ is the sign (positive or negative) of y , is the simplest axial stretching distortion, giving displacements of

$$y' - y = \Delta y = b \operatorname{sgn}(y) y^2, \tag{A.9}$$

and Fig. 1a applies. Since the displacements are wholly in y , the greatest signal losses will accrue for terms far from the equator (large Z).

A.3. Twist

As with stretch, a linearly changing twist in a tube:

$$\varphi' = \varphi_0 + fy \tag{A.10}$$

(where φ' refers to the azimuthal rotation of the actual tube and φ_0 refers to the undistorted model) represents a misalignment of the axial repeat distance, not a distortion. Once again, the distortion is

at least a second-order effect:

$$\varphi' = \varphi_0 + f \operatorname{sgn}(y) y^2, \tag{A.11}$$

giving

$$\varphi' - \varphi_0 = \Delta\varphi = f \operatorname{sgn}(y) y^2. \tag{A.12}$$

Instead of calculating the Δx and Δy displacements this causes, we can calculate directly the effect on the phases of the Fourier terms: the phase error ($\Delta\phi$; Eq. (1)) on a Bessel order n layer-line, due to an azimuthal misalignment of $\Delta\varphi$, is $n \Delta\varphi$. So the signal retention on that layer-line can be calculated as

$$\text{Fraction retained} = \frac{1}{\ell} \int_{-\ell/2}^{\ell/2} \cos(nfy^2) dy. \tag{A.13}$$

This is the same integral as Eq. (4) (plotted in Fig. 1a), except that the Bessel order, n , replaces the factor $2\pi/\lambda$ within the cosine's argument. At 5 Å resolution $2\pi/\lambda$ is only 1.25. However, the maximum value of n at this resolution can be high (e.g. 430 for an ACh receptor tube), so very small displacements in twist may be amplified by high Bessel orders into having a large effect.

A.4. Variable tilt

Unlike the previous examples, a linearly changing tilt angle:

$$\omega' = \omega_0 + ty \tag{A.14}$$

is a distortion, representing bend out of the object plane, and gives a phase error (see [26]):

$$\Delta\phi = n \left(\arctan \left(\frac{Z \sin \omega_0}{X} \right) - \arctan \left(\frac{Z \sin(\omega_0 + ty)}{X} \right) \right), \tag{A.15}$$

where Z and X are the reciprocal distances along and perpendicular to the meridian in the transform, respectively. The signal retention is therefore:

$$\text{Fraction retained} = \frac{1}{\ell} \int_{-\ell/2}^{\ell/2} \cos \left(n \left(\arctan \left(\frac{Z \sin \omega_0}{X} \right) - \arctan \left(\frac{Z \sin(\omega_0 + ty)}{X} \right) \right) \right) dy. \tag{A.16}$$

The phase errors and signal loss are greatest when ω_0 is zero. Assuming that ω_0 is close to zero and that the change in tilt ($= ty$) is small, the signal retention can be approximated as

$$\begin{aligned} \text{Fraction retained} &= \frac{1}{\ell} \int_{-r/2}^{r/2} \cos\left(\frac{-nZty}{X}\right) dy \\ &= \frac{2X \sin\left(\frac{nZt\ell}{2X}\right)}{nZ\ell}. \end{aligned} \quad (\text{A.17})$$

The relation between signal retention and segment length is typical of a first-order distortion, and is plotted in Fig. 1c. The signal retention drops much more quickly than it would for a second-order distortion (Fig. 1b), but with short segments most of the signal is retained. The loss of signal is worst near the beginning of each layer-line (low X), but improves further along the layer-line (larger X). In fact, the signal loss from variable tilt is more concentrated in a small part of the transform than is the case with most other distortions, being most pronounced in terms with high Z and n/X values.

A.5. Shear

A constant shear perpendicular to the axis of the tube is also a first-order distortion, and may be described as

$$y' = y, \quad (\text{A.18})$$

$$x' = x + ay, \quad (\text{A.19})$$

where the factor a describes the amount of shear. In practice, however, a shear perpendicular to the tube axis is treated by the programs as a rotation of the tube in the image plane. If the tube is rotated back so that its axis once again lies on the y axis, the shear will now look like

$$y' = y + x \frac{a}{\sqrt{1+a^2}}, \quad (\text{A.20})$$

$$x' = \frac{x}{\sqrt{1+a^2}}. \quad (\text{A.21})$$

That is, by rotating the tube, the shear is converted from being perpendicular to the tube axis into being parallel, with a smaller magnitude. The ap-

parent scale change in the x -direction (Eq. (A.21)) will be absorbed in the r_{scale} parameter, so the total displacement and signal loss will be in the y -direction only:

$$\Delta y = x \frac{a}{\sqrt{1+a^2}}. \quad (\text{A.22})$$

Δy is a function of x , not y , so the signal retention can be expressed as

$$\begin{aligned} \text{Fraction retained} &= \int_{x=-r}^r \cos\left(\frac{2\pi ax}{\lambda_y \sqrt{1+a^2}}\right) dx \\ &= \frac{\lambda_y \sqrt{1+a^2}}{2\pi ar} \sin\left(\frac{2\pi ar}{\lambda_y \sqrt{1+a^2}}\right), \end{aligned} \quad (\text{A.23})$$

where r represents the radius of the tube times r_{scale} . The signal retention is independent of segment length. Eq. (A.23) shows that unless ar is larger than $\sim 0.5 \text{ \AA}$ (in which case the shear is likely to be noticed and the tube discarded), almost 100% of the signal will be retained at 5 \AA resolution without further corrections being necessary.

A.6. Flattening

An unflattened tube can be thought of as a set of concentric cylinders, each representing the mass at a given radius from the tube axis. When flattened, each of these cylinders may be thought of as having been squeezed to become elliptical in cross-section. The length of the major axis of the ellipse will be

$$a(r) = r_{\text{scale}}(r)r, \quad (\text{A.24})$$

where r refers to the radius of the unflattened cylinder and $r_{\text{scale}}(r)$ is the flattening ratio at that radius. The flattening ratio should change with radius to keep the distances between the concentric cylinders constant before and after flattening. That is, if one cylinder has a radius of 250 \AA and the other has a radius of 380 \AA , then the major axes of the ellipses they flatten into must also differ in length by 130 \AA . So, given the flattening ratio at one radius ($r_{\text{scale}}(r_0)$ for the radius r_0), we can calculate the r_{scale} for any other:

$$r_{\text{scale}}(r) = 1 + \frac{r_0}{r} (r_{\text{scale}}(r_0) - 1). \quad (\text{A.25})$$

At r_{scales} near 1, the flattening of any one concentric cylinder will approximate a change in x -direction scaling:

$$x' = \frac{r_{\text{scale}}(r)}{r_{\text{scale}}(r_0)} x, \quad (\text{A.26})$$

where x is the expected position of a point on the cylinder, x' is its real position after flattening, and the scaling change, $r_{\text{scale}}(r)$, is a function of the radius of the concentric cylinder. The $r_{\text{scale}}(r_0)$ in the denominator is a partially corrective demagnification which will be performed automatically by the analysis programs, because they interpret a flattening of the tube as an increased magnification in the x -direction. We are allowed to call this apparent increase in magnification $r_{\text{scale}}(r_0)$ if we pick the proper radius r_0 for Eq. (A.25), so that $r_{\text{scale}}(r_0)$ equals the apparent increase.

Hence, the flattening-induced displacement,

$$\Delta x(x, r) = x' - x = x \left(\frac{r_{\text{scale}}(r)}{r_{\text{scale}}(r_0)} - 1 \right), \quad (\text{A.27})$$

is a function of both x and r , the radius of the unflattened concentric cylinder. To calculate the fraction of signal retained, we should integrate over both of these parameters when applying Eq. (2):

$$\begin{aligned} \text{Fraction retained} &= \frac{2}{r_{\text{max}}^2 - r_{\text{min}}^2} \int_{r_{\text{min}}}^{r_{\text{max}}} dr \\ &\times \int_0^r \cos \left(\frac{2\pi x \left(\frac{r_{\text{scale}}(r)}{r_{\text{scale}}(r_0)} - 1 \right)}{\lambda_x} \right) dx \\ &= \frac{2}{r_{\text{max}}^2 - r_{\text{min}}^2} \int_{r_{\text{min}}}^{r_{\text{max}}} dr \\ &\times \int_0^r \cos \left(\frac{2\pi x (r - r_0) (1 - r_{\text{scale}}(r_0))}{\lambda_x r_{\text{scale}}(r_0) r} \right) dx, \quad (\text{A.28}) \end{aligned}$$

where r_{max} and r_{min} refer to the outer and inner radii of the unflattened tube. The fractional signal retention is plotted as a function of $r_{\text{scale}}(r_0)$ in Fig. 1d.

References

- [1] A. Brisson, P.N.T. Unwin, *J. Cell Biol.* 99 (1984) 1201.
- [2] C. Toyoshima, H. Sasabe, D.L. Stokes, *Nature* 362 (1993) 469.
- [3] M.F. Schmid, J.P. Robinson, B.R. Das Gupta, *Nature* 364 (1993) 827.
- [4] A. Polyakov, E. Severinova, S.A. Darst, *Cell* 83 (1995) 365.
- [5] T. Akiba, C. Toyoshima, T. Matsunaga, M. Kawamoto, T. Kubota, K. Fukuyama, K. Namba, H. Matsubara. *Nature Struct. Biol.* 3 (1996) 553.
- [6] G. Tsiotis, T. Walz, A. Spyridaki, A. Lustig, A. Engel, D. Ghanotakis, *J. Mol. Biol.* 259 (1996) 241.
- [7] C. Toyoshima, N. Unwin, *Ultramicroscopy* 25 (1988) 279.
- [8] R. Henderson, J.M. Baldwin, K.H. Downing, J. Lepault, F. Zemlin, *Ultramicroscopy* 19 (1986) 147.
- [9] R. Henderson, J.M. Baldwin, T.A. Ceska, F. Zemlin, E. Beckmann, K.H. Downing, *J. Mol. Biol.* 231 (1990) 899.
- [10] W. Kuhlbrandt, D.N. Wang, Y. Fujiyoshi, *Nature* 367 (1994) 614.
- [11] C. Toyoshima, N. Unwin, *J. Cell Biol.* 111 (1990) 2623.
- [12] E.H. Egelman, *Ultramicroscopy* 19 (1986) 367.
- [13] M. Whittaker, B.O. Carragher, R.A. Milligan, *Ultramicroscopy* 58 (1995) 245.
- [14] J.D. Jontes, E.M. Wilson-Kubalek, R.A. Milligan. *Nature* 378 (1995) 751.
- [15] T.-W. Jeng, R.A. Crowther, G. Stubbs, W. Chiu, *J. Mol. Biol.* 205 (1989) 251.
- [16] T. Ogawa, X. Yu, A. Shinohara, E.H. Egelman, *Science* 259 (1993) 1896.
- [17] M. Kikkawa, T. Ishikawa, T. Wakabayashi, N. Hirokawa, *Nature* 376 (1995) 274.
- [18] K. Hirose, A. Lockhart, R.A. Cross, L.A. Amos. *Nature* 376 (1995) 277.
- [19] D.G. Morgan, D. DeRosier, *Ultramicroscopy* 46 (1992) 263.
- [20] D.G. Morgan, C. Owen, L.A. Melanson, D.J. DeRosier, *J. Mol. Biol.* 249 (1995) 88.
- [21] D.A. Bluemke, B. Carragher, R. Josephs, *Ultramicroscopy* 26 (1988) 255.
- [22] N. Unwin, *J. Mol. Biol.* 229 (1993) 1101.
- [23] N. Unwin, *Nature* 373 (1995) 37.
- [24] R. Beroukhim, N. Unwin, *Neuron* 15 (1995) 323.
- [25] K. Tani, H. Sasabe, C. Toyoshima, *Ultramicroscopy* 65 (1996) 31.
- [26] D.J. DeRosier, P.B. Moore, *J. Mol. Biol.* 52 (1970) 355.
- [27] T. Wakabayashi, H.E. Huxley, L.A. Amos, A. Klug, *J. Mol. Biol.* 93 (1975) 477.
- [28] L.A. Amos, A. Klug, *J. Mol. Biol.* 99 (1975) 51.
- [29] A. Klug, F.H.C. Crick, H.W. Wyckoff, *Acta Crystallogr.* 11 (1958) 199.
- [30] E. Kubalek, S. Ralston, J. Lindstrom, N. Unwin, *J. Cell Biol.* 105 (1987) 9.
- [31] N. Unwin, *J. Mol. Biol.* 257 (1996) 586.